# Fluid and kinetic nonlinearities of near-acoustic plasma waves (EP)

M. Affolter (iD), F. Anderegg (iD), D. H. E. Dubin, F. Valentini (iD), and C. F. Driscoll

## COLLECTIONS

(EP) This paper was selected as an Editor's Pick

View Online  Export Citation  CrossMark

## ARTICLES YOU MAY BE INTERESTED IN

# Fluid and kinetic nonlinearities of near-acoustic plasma waves EP

View Online　　Export Citation　　CrossMark

M. Affolter,[1] iD F. Anderegg,[1] iD D. H. E. Dubin,[1] F. Valentini,[2] iD and C. F. Driscoll[1]

**AFFILIATIONS**

[1]Department of Physics, University of California at San Diego, La Jolla, California 92093, USA
[2]Dipartimento di Fisica, Università della Calabria, I-87036 Rende, CS, Italy

**ABSTRACT**

Large amplitude, near-acoustic plasma waves have a temperature-dependent harmonic content and nonlinear frequency shifts. On cold plasmas, experiments show that fluid nonlinearities dominate, and the observed harmonic content is well predicted by a recent fluid analysis. In contrast, the measured nonlinear frequency shift is smaller than this theory prediction, suggesting the presence of other nonlinear effects neglected in this analysis. When the plasma is heated, kinetic effects become important, and we observe an increase in both the harmonic content and nonlinear frequency shift. Quantitative experiments on the stability of these large amplitude, near-acoustic plasma waves strongly support the idea that trapped particles reduce the amplitude threshold for instability below fluid models. At low temperatures, the broad characteristics of the parametric instability are determined by the frequency detuning of the pump and daughter wave and the wave-wave coupling strength, surprisingly consistent with simple cold fluid, three-wave theories. However, at higher temperatures, the pump wave becomes unstable at half the threshold pump wave amplitude, with similar exponential growth rates as for a cold plasma.

*Published under license by AIP Publishing.* https://doi.org/10.1063/1.5129529

## I. INTRODUCTION

In plasmas, waves are commonly driven to large amplitudes either through internal or external processes where they exhibit nonlinear behavior. Strong mode coupling creates wave harmonics, which generally steepen the density perturbation,[1–4] and the frequency of these large amplitude waves is shifted away from the linear frequency.[4–8] A myriad of instabilities also generally make these large amplitude waves unstable. One common type of instability, the parametric instability, has been widely investigated theoretically[4,9–14] and has been observed in tokamaks,[15–18] non-neutral plasmas,[8,19–21] high-intensity laser experiments,[22,23] and other devices.[24,25] The parametric decay of ion acoustic waves (IAWs) has been postulated[26–30] as a possible cause for the saturation of stimulated Brillouin scattering observed in high-intensity laser experiments.[22,23,31–34] However, quantitative measurements of nonlinear, near-acoustic waves are lacking, especially on the influence of fluid vs kinetic effects.

In this paper, we present quantitative measurements of the harmonic content, frequency, and stability of nonlinear Trivelpiece-Gould (TG) waves on well-controlled, laser-diagnosed, pure ion plasmas. These plasma waves are azimuthally symmetric standing waves with a near-acoustic (i.e., nearly dispersion-free) linear dispersion relation discretized by the axial wavenumber $k_z = m_z(\pi/L_p)$. A wide range of temperatures and, hence, the ratio of thermal velocity $\bar{v}$ to

phase velocity $v_\phi$ are explored in order to investigate the effects of both fluid and kinetic nonlinearities.

Due to the near-acoustic nature of these TG waves, harmonics of the fundamental are nearly on the linear dispersion relation and thus are driven resonantly through nonlinear mode coupling. We find that the measured harmonic amplitude $|A_m^{(j)}|$ is proportional to the fundamental wave amplitude $|A_m^{(1)}|$ to the $j$th power, where $j$ is the harmonic number. At low temperatures, the harmonic amplitude increases in rough agreement with cold fluid theory[4] when the deviation from acoustic dispersion,

$$\Delta_{mj} \equiv j\omega_m - \omega_j, \tag{1}$$

is reduced. In contrast, at higher temperatures, the harmonic content is larger than the cold fluid prediction, suggesting an influence of kinetic effects.

The fundamental mode frequency is also observed to be shifted away from the linear frequency as the wave amplitude is increased. Cold fluid theory[4] predicts a positive nonlinear frequency shift that is proportional to the amplitude of the second harmonic $|A_m^{(2)}|$. However, experimentally, we observe a smaller nonlinear frequency shift, which is negative in certain cases, suggesting the presence of other nonlinear effects not included in this fluid analysis. As the plasma temperature is increased, this nonlinear frequency shift increases.

At these large wave amplitudes, a simple three-wave fluid analysis[35] predicts that an $m_z = 2$ pump wave will decay through a parametric instability to two longer wavelength, $m_z = 1$ daughter waves. At low temperatures ($v_\phi/\bar{v} \gtrsim 5$), the broad characteristics of the observed instability are consistent with this simple three-wave theory, parameterized by the frequency detuning between the pump and daughter wave $\Delta_{12}$ and scaled pump wave amplitude $\Gamma_0$. Here, $\Gamma_0 \equiv |A_2^{(1)}|\omega_1(3R/8)$, where $|A_2^{(1)}|$ is the fundamental amplitude of the pump wave and

$$R \equiv \frac{2}{k_\perp R_p} J_1(k_\perp R_p) \qquad (2)$$

is a scaling factor[4] that is dependent on the transverse wavenumber $k_\perp$ and plasma radius $R_p$. For the plasmas discussed here, $R \sim 0.85$. When the pump wave amplitude is above the threshold ($\Gamma_0 \gtrsim \Delta_{12}/2$), the parametric instability is observed. The daughter wave amplitude grows exponentially at a rate $\Gamma_E \sim \Gamma_0$ with "phase-locked" frequency $\omega_1 = \omega_2/2$ and relative phase $\theta_{12} \sim -\arccos(-\Delta_{12}/2\Gamma_0)$, consistent with three-wave instability analyses.[35,36] For small pump wave amplitudes ($\Gamma_0 \lesssim \Delta_{12}/2$), the relative wave phase varies as $\theta_{12} \propto \omega_B t$, causing the daughter wave amplitude to "bounce" as $A_B \sin(\omega_B t)$ with $\omega_B \sim \Delta_{12}$ and $A_B \propto \Gamma_0$, in quantitative agreement with three-wave theory.[35,36] Experimentally, we typically observe a slow average growth of this modulated daughter wave, which is not predicted by fluid theory.

When harmonics of the pump and daughter wave are included in a more sophisticated N-wave analysis of the instability,[4] the parametric instability is suppressed. This fluid theory[4] predicts that traveling pump waves of any amplitude are stable with respect to parametric (three-wave) processes, analogous to the stability of solitary-wave solutions of the Korteweg-de-Vries[37] and Boussinesq[38] equations. A recent analysis[39] shows that traveling pump waves can be weakly unstable to higher order wave processes (4-wave, 5-wave, etc.) over narrow wavenumber bands associated with N-wave resonances ($N > 3$), similar to the instabilities predicted for deep water waves.[40,41] In contrast, for the standing waves of interest in these experiments, the instability threshold is pushed to larger pump wave amplitudes with weaker growth rates.[4] Although the observed harmonics are consistent with this N-wave fluid analysis, the predicted suppression of the parametric instability is not.

A recent kinetic theory[42] reconciles this discrepancy by including a novel effect of particles trapped in the wave potential. Even for these experimentally low temperatures ($v_\phi/\bar{v} \gtrsim 5$), there can be a trapped particle population if the wave amplitude is sufficiently large to reach back into the velocity distribution. These trapped particles are predicted to destabilize the wave because they exhibit negative compressibility: when compressed (or expanded) by the wave motion associated with the instability, the trapped particle pressure and density decrease (or increase), and this leads to a loss of the stability when the trapped particle fraction is sufficiently large, i.e., $f_T \gtrsim 0.1\%$. This trapped particle mechanism is a general phenomenon that could play a role in other nonlinear systems, such as nonlinear IAWs where kinetic simulations[28,43] show instability thresholds below fluid theory predictions.

To investigate this trapped particle mechanism, experiments are conducted at higher temperatures ($v_\phi/\bar{v} \lesssim 5$) where a larger fraction of particles interact resonantly with the wave potential. For a linear wave with phase velocity $v_\phi \equiv \omega/k_z$ and a Maxwellian particle

distribution $F(r,z,v,t)$, the fraction of resonant particles scales as $f_T \sim (v_\phi/\bar{v})^4 \exp(-v_\phi^2/\bar{v}^2)$ with $\bar{v}^2 \equiv T/M$ and $f_T > 10^{-9}$ for ($v_\phi/\bar{v} \lesssim 5$) corresponding to $T \gtrsim 0.3$ eV. As the plasma temperature and thus the fraction of trapped particles are increased, a reduction in the instability threshold is observed in qualitative agreement with recent kinetic theory.[42] Relative to cold plasmas, warm plasmas exhibit similar exponential growth rates at half the pump wave amplitude. We also present new (r, z, $v_z$) drift-kinetic Poisson and (r, z) particle-in-cell (PIC) simulations, which are unstable near the experimental pump wave amplitudes only when trapped particles are included.

## II. EXPERIMENTAL APPARATUS

Figure 1 shows a schematic of the experimental apparatus[44] used to confine and diagnose these cylindrical, predominantly $Mg^+$ ion plasmas. To confine the ions axially, positive potentials $V_c$ are applied to the end rings of the Penning-Malmberg trap, and radial confinement is provided by a 3 T, axial magnetic field. A weak "rotating wall" (RW) perturbation, applied to the 8-sectored ring shown in Fig. 1, maintains the plasma in a near thermal equilibrium state described by "top-hat" density and rigid-rotor rotation profiles.

Radial profiles of the density $n(r)$, plasma temperature $T(r)$, and rotation velocity $v_\theta(r)$ are measured at the axial location $z_L$ of the photon viewing volume through Laser Induced Fluorescence (LIF) techniques.[44] A typical plasma has a radius $R_p \sim 0.5$ cm and a uniform density $n_0 \sim 2 \times 10^7$ cm$^{-3}$ and rotates at $f_E \sim 10$ kHz. Laser cooling and cyclotron heating on $^{24}Mg^+$ control the plasma temperature over a range $10^{-3} \lesssim T \lesssim 0.62$ eV corresponding to $90 \gtrsim v_\phi/\bar{v} \gtrsim 3.5$.

A (r, z) Poisson-Boltzmann solver extends these measured radial cross sections to determine the plasma length. This solver iterates the (r, z) density $n(r, z)$ to establish a self-consistent solution of Poisson's equation

$$\nabla^2 \phi(r,z) = -4\pi q n(r,z), \qquad (3)$$

subject to the boundary conditions at $r = R_w$ of the experimental confining potentials. The z-boundary condition is taken to be $\partial\phi/\partial z = 0$ at $z = \pm z_E$, where $z_E$ is well beyond the plasma end. Local thermal equilibrium along the magnetic field (i.e., along $\hat{z}$) is assumed, so that the density is

$$n(r,z) = G(r) \exp[-q\phi(r,z)/T(r)], \qquad (4)$$

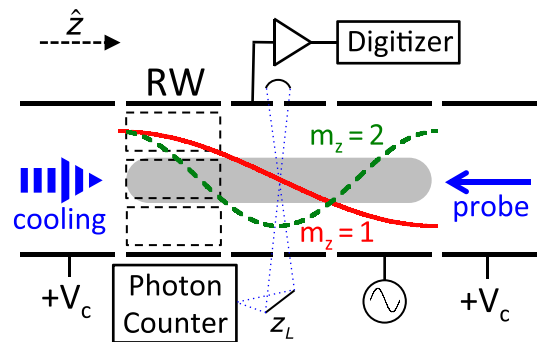where $G(r)$ is constrained by the measured $n(r)$.



**FIG. 1.** Schematic of the 3 T Penning-Malmberg trap used to confine and diagnose these multispecies ion plasmas and a sketch of the first two axial modes.

Equation (3) is solved numerically on a $512 \times 1024$ grid using an iterative calculation. Initially, the plasma is assumed to be a rod of charge $n(r, 0 \leq z \leq L_c) = n(r)$ extending the length of the confining volume $L_c$. This initial guess is used with the boundary conditions to determine $\phi(r, z)$, which then determines a new guess of $n(r, z)$. A fraction of this new $n(r, z)$ solution is added to the old solution while maintaining the constraint that $n(r, z_L) = n(r)$. This process is repeated until the maximum density change is less than 0.01%. The resulting solutions are cylindrical plasmas with rounded ends. Experimentally, the on-axis plasma length is varied over the range $12.4 \lesssim L_p \lesssim 20.3$ cm by changing the confinement potentials and length of the confinement volume.

## III. LINEAR WAVE FREQUENCIES

In these trapped plasmas, the linear dispersion relation of Langmuir waves is near-acoustic because of the shielding from the radial boundary at $R_w = 2.86$ cm. The Trivelpiece-Gould dispersion relation[45] for z-periodic waves on an infinite-length column is

$$\omega(k_z) = \omega_p \frac{k_z}{\sqrt{k_z^2 + k_\perp^2}} \left[ 1 + \frac{3}{2} \left( \frac{\bar{v}}{v_\phi} \right)^2 \right], \qquad (5)$$

where $k_z = m_z(\pi/L_p)$ and $\omega_p = \sqrt{4\pi e^2 n_0/M}$ is the plasma frequency. The transverse wavenumber $k_\perp$ is determined by the condition that the axial and radial plasma/vacuum electric fields be continuous at the plasma radius,[45] which is set by

$$k_\perp R_p \frac{J_1(k_\perp R_p)}{J_0(k_\perp R_p)} = -k_z \frac{S_r(k_z, R_p, R_w)}{S_z(k_z, R_p, R_w)} \qquad (6)$$

for axisymmetric $m_\theta = 0$ modes in a strong magnetic field. Here,

$$S_z = I_0(k_z R_p) K_0(k_z R_w) - I_0(k_z R_w) K_0(k_z R_p) \qquad (7)$$

and

$$S_r = I_1(k_z R_p) K_0(k_z R_w) + I_0(k_z R_w) K_1(k_z R_p) \qquad (8)$$

are related to the axial and radial vacuum electric field solutions at $R_p$, respectively. For long, thin plasmas with $k_\perp R_p \ll 1$ and $k_z R_w \ll 1$, Eq. (6) reduces to $k_\perp \sim R_p^{-1} \sqrt{2/\ln(R_w/R_p)}$ a constant, independent of the axial wave number. However, for the plasmas of these experiments, Eq. (6) determines $k_\perp \sim 0.9 R_p^{-1} + 0.5 k_z$.

These waves are excited from a confinement ring located near the plasma end, and the resulting wave is detected as an image charge induced voltage $V_w$ on an off-center ring, as shown in Fig. 1. Typically, a 40 cycle sine wave drive with an amplitude $A_D \sim 2 - 200$ mV$_{pp}$ is used. The drive is ramped to/from full amplitude over four cycles to minimize the direct excitation of other waves, and the largest drives generally heat the plasma by $\Delta T \sim 10^{-2}$ eV. The mode amplitudes are obtained by fitting the digitized wall signal in time segments of approximately five wave cycles with sine waves near the linear mode frequencies.

Figure 2 shows the frequency measurements of several small amplitude TG modes for two different plasma lengths. The measured mode frequencies (symbols) are nearly acoustic (dashed lines), and the deviation from acoustic dispersion $\Delta_{12}/\omega_1$ is dependent on the plasma geometry, i.e., $L_p/R_p$. When the plasma length is increased from 13.6 cm to 20.3 cm (blue to red data), the relative deviation from
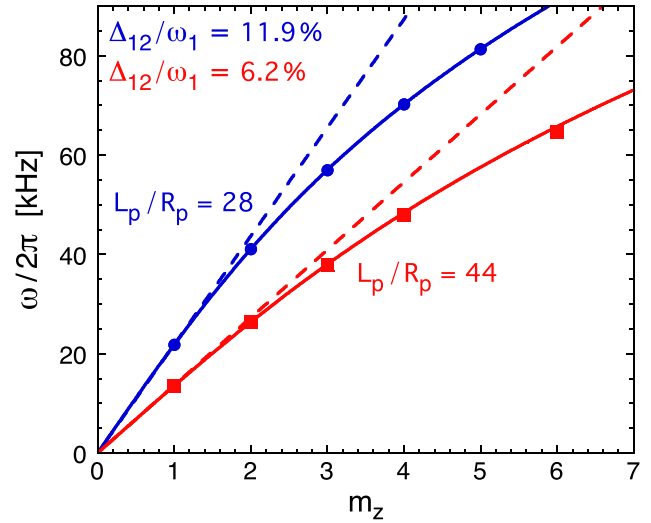


**FIG. 2.** Measured frequencies of standing TG waves (symbols) for two different plasma lengths on very cold plasmas with $v_\phi/\bar{v} \sim 90$. Solid curves are one parameter fits to Eq. (5), and dashed lines show acoustic dispersion.

acoustic dispersion $\Delta_{12}/\omega_1$ is reduced by about 50%. Increasing the plasma length $12.4 \lesssim L_p \lesssim 20.3$ cm decreases the mode frequencies $23.8 \gtrsim \omega_1/2\pi \gtrsim 13.65$ kHz and decreases the relative detunings $3.1 \gtrsim \Delta_{12}/2\pi \gtrsim 0.85$ kHz.

Since $k_\perp$ is an increasing function of $k_z$ for these plasmas, the deviation from acoustic dispersion is larger than predicted by the typical constant $k_\perp$ approximation. Fairly good agreement between all the measured mode frequencies (symbols) and Eq. (5) (solid curves) is obtained when $k_\perp$ is properly determined from Eq. (6), and the plasma length is used as a fit parameter. These fits give plasma lengths within a few percent of the lengths determined from the (r, z) Poisson-Boltzmann solver. In contrast, the constant $k_\perp$ approximation of Eq. (6) underestimates $\Delta_{12}/\omega_1$ by about a factor of 4 for these plasmas.

## IV. NONLINEAR WAVE STRUCTURE

The near-acoustic nature of these TG waves allows for strong mode couplings. Harmonics of the fundamental wave are nearly on the linear dispersion relation and thus are driven resonantly by the fundamental through nonlinear mode coupling. For large amplitude waves, we find

$$V_w(t) = \sum_j A_m^{(j)} \cos(j\omega_m t), \qquad (9)$$

where $j = 1, 2, 3, \ldots$ correspond to the phase-locked frequency harmonics of the fundamental and $|A_m^{(j)}|$ is the fractional density perturbation of harmonic $j$ with frequency $j\omega_m$. Since $V_w(t)$ is measured on a single axial electrode, we are unable to determine the axial mode structure of these waves. In this work, we keep only the spatial Fourier harmonics with the $\cos(jk_z z)$ axial dependence for frequency $j\omega_m$ and thus a nonlinear density eigenfunction

$$\Psi_m = \sum_j \Psi_m^{(j)}, \qquad (10)$$

where

$$\Psi_m^{(j)} = \frac{1}{2} A_m^{(j)}(t) n_0 e^{-ij\omega_m t} \cos\left(jk_z z\right) J_0(k_\perp r) + c.c. \quad (11)$$

for a top-hat density profile. This assumption is supported by recent cold fluid theory,[4] which predicts that the nonlinear amplitude is dominated by the near dispersion harmonics with an $e^{-ij\omega_m t}\cos\left(jk_z z\right)$ dependence for the modes considered here.

We characterize the size of these nonlinear waves by the fractional density perturbation of the fundamental $A_m \equiv A_m^{(1)}$, which is directly related to the measured amplitude of $V_w$ at $\omega_m$ through Gauss's Law

$$A_m = \left[\frac{(k_z^2 + k_\perp^2)k_z C \mathcal{S}_z(k_z, R_p, R_w)}{2\pi e n_0 J_0(k_\perp R_p)\hat{f}}\right] V_w. \quad (12)$$

Here, $C$ is the capacitance of the detection ring extending axially from position $z_1$ to $z_2$, and $\hat{f} = \sin\left(k_z z_2\right) - \sin\left(k_z z_1\right)$ is the finite overlap of the detection ring and plasma wave. Equation (12) reduces to Eq. (2) of Ref. 46 for long, thin plasmas. The typical uncertainty in the plasma length $\delta L_p/L_p \sim 5\%$, radius $\delta R_p/R_p \sim 5\%$, and equilibrium density $\delta n_0/n_0 \sim 2\%$ results in a 10% uncertainty in the conversion of $V_w$ to $|A_1|$ and a 20% uncertainty in $|A_2|$ and $|A_3|$. By replacing $k_z$ in Eq. (12) with $jk_z$, the measured amplitude of $V_w$ at $j\omega_m$ is converted to $|A_m^{(j)}|$.

Shown in Fig. 3(a) is the detected temporal waveform of a large amplitude $m_z = 1$ mode for a typical cold plasma $T \sim 10^{-2}$ eV with $\Delta_{12}/\omega_1 = 11.9\%$. The wave density perturbation (black curve) includes the fundamental (red curve), second ($j=2$), and third ($j=3$) frequency harmonics. Higher harmonics $j > 4$ are not well coupled to the wall and are typically not detectable above the experimental noise floor. Figure 3(a) shows that harmonic generation steepens the fundamental density perturbation away from a sinusoid, and for this case, it increases the peak density perturbation by about a factor of 2. Similar steepened waveforms were observed in previous experiments investigating Bernstein–Greene–Kruskal (BGK) modes and solitons in pure electron plasmas[2] and are predicted by cold fluid theory.[4,39]

The amplitude of these harmonics is dependent on the size of the fundamental density perturbation and on the deviation from acoustic dispersion. Figure 3(b) shows the amplitude measurements of the second and third harmonics vs the fundamental amplitude as the wave damps. The harmonic amplitude $|A_1^{(j)}|$ is proportional to $|A_1|$ to the $j$th power. We also observe a larger harmonic content for more acoustic dispersion relations. When $\Delta_{12}/\omega_1$ is reduced by about 50%, the amplitude of the second harmonic $|A_1^{(2)}|$ increases by a factor of 2, and the third harmonic amplitude $|A_1^{(3)}|$ increases by a factor of 4.

These results are in agreement with cold fluid theory.[4] This theory keeps the nonlinear convective terms in the cold fluid equations and solves for the nonlinear density, velocity, and frequency of these standing waves using a perturbation expansion, assuming that the fundamental wave amplitude $|A_m|$ is small. The predicted second and third order corrections to the nonlinear wave density are

$$|A_1^{(2)}| = \frac{3}{8}\left[\frac{1}{1 - (\omega_2/2\omega_1)^2}\right] R(|A_1|)^2$$
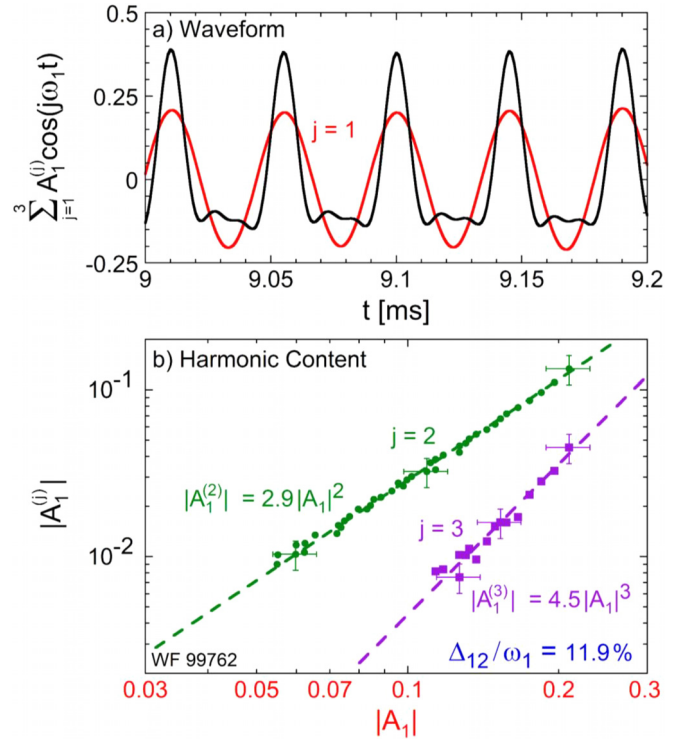$$\approx \frac{3}{8}\frac{\omega_1}{\Delta_{12}} R(|A_1|)^2 \quad (13)$$

and



**FIG. 3.** (a) Density perturbation (black curve) of a large amplitude $m_z = 1$ TG mode from measurements of the image charge induced wall voltage. Harmonic generation steepens and increases the fundamental density perturbation (red curve). (b) Measured amplitude (symbols) of the frequency harmonics $j=2$ and $j=3$ of this nonlinear $m_z = 1$ mode. Fits (dashed lines) show that the amplitude of the harmonics is proportional to fundamental amplitude to the $j$th power.

$$|A_1^{(3)}| = \frac{1}{32}\left[\frac{5 + (\omega_2/\omega_1)^2}{\left\{1 - (\omega_2/2\omega_1)^2\right\}\left\{1 - (\omega_3/3\omega_1)^2\right\}}\right] R^2(|A_1|)^3$$
$$\approx \frac{27}{64}\frac{\omega_1}{\Delta_{12}}\frac{\omega_1}{\Delta_{13}} R^2(|A_1|)^3, \quad (14)$$

respectively, where the approximations assume that $\Delta_{12}/\omega_1$ and $\Delta_{13}/\omega_1$ are small.

The measured (symbols) and predicted (solid lines) scaling factors for $|A_1^{(2)}|$ and $|A_1^{(3)}|$ are shown in Fig. 4 for cold plasmas $T \sim 10^{-2}$ eV with a range $6.2\% \lesssim \Delta_{12}/\omega_1 \lesssim 13.0\%$. As the plasma becomes more acoustic, the measured amplitudes of the second [Fig. 4(a)] and third [Fig. 4(b)] harmonic increase linearly with $\omega_1/\Delta_{12}$ and $(\omega_1/\Delta_{12})(\omega_1/\Delta_{13})$, respectively, in qualitative agreement with theory. However, theory underestimates $|A_1^{(2)}|$ and overestimates $|A_1^{(3)}|$ by about 20%.

So far, these experimental results have only considered cold plasmas. As the plasma temperature is increased from $10^{-2}$ to 0.55 eV, the linear dispersion relation becomes more acoustic with $\Delta_{12}/\omega_1$ and $\Delta_{13}/\omega_1$ decreasing by about a factor of 1.2 for a plasma with $\Delta_{12}/\omega_1 = 11.9\%$ at $T \sim 10^{-2}$ eV. This decrease would suggest $1.2\times$ and $1.4\times$ increases in the amplitude of the second and third harmonics, respectively. However, $|A_1^{(2)}|$ is observed to increase by a factor of 1.6, and $|A_1^{(3)}|$ is increased by a factor of 2.7. These results suggest that
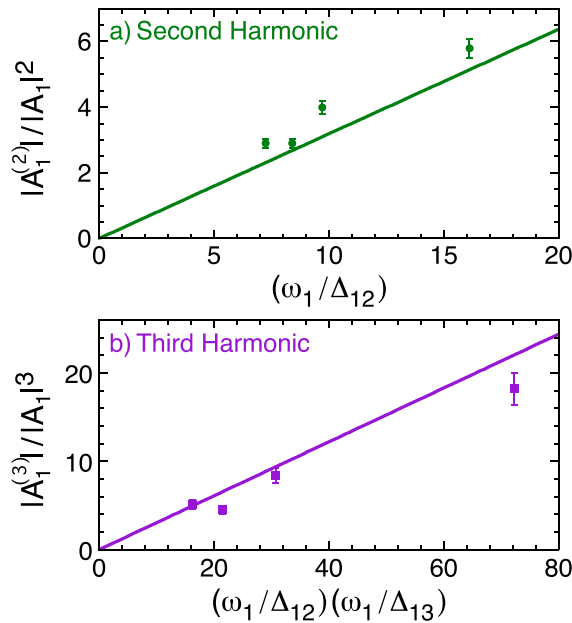
**FIG. 4.** (a) The measured amplitude (symbols) of the second harmonic of a large amplitude $m_z = 1$ wave increases linearly with $\Delta_{12}/\omega_1$ as predicted by theory (solid line), but it is about 20% larger in magnitude. (b) In contrast, the measured third harmonic amplitude (symbols) is about 20% smaller than theory (solid line).



**FIG. 5.** Measurements of the percent change in the frequency of a large amplitude $m_z = 1$ wave immediately after (solid symbols) or during (open symbols) the driving burst vs the square of the fundamental wave amplitude for both cold (a) and warm plasmas (b). Dashed lines are fits to the wave amplitude squared.

kinetic effects, which are neglected in the cold fluid analysis, may cause further steepening of the wave density perturbation.

## V. NONLINEAR FREQUENCY SHIFTS

Along with the generation of harmonics, nonlinear theory[4] predicts that the frequency of these large amplitude TG waves is shifted away from the linear dispersion relation. Following the same perturbation expansion of the nonlinear cold fluid equations discussed in Sec. IV, theory predicts a second order correction to the linear standing wave frequency of

$$\frac{\delta\omega_1}{\omega_1} = \frac{1}{64}\left[\frac{\{1-(\omega_1/\omega_2)^2\}\{(\omega_2/\omega_1)^2+8\}}{1-(\omega_2/2\omega_1)^2}\right]R^2(|A_1|)^2$$

$$\approx \frac{9}{64}\frac{\omega_1}{\Delta_{12}}R^2(|A_1|)^2, \qquad (15)$$

where, again, the approximation assumes that $\Delta_{12}/\omega_1$ is small. Previous simulations of IAWs[6] have shown a similar $|A_1|^2$ scaling for the frequency shift.

Figure 5(a) shows the measured percent change in the frequency of a large amplitude $m_z = 1$ wave vs $|A_1|^2$ for two cold plasmas $T \sim 10^{-2}$ eV with different $\Delta_{12}/\omega_1$ values. To avoid conflating thermal and amplitude effects as the wave damps, the wave frequency is measured immediately after the driving burst is turned off (solid symbols) or in short time segments as the wave is driven to large amplitude (open symbols). The measured mode frequency increases as $|A_1|^2$ (dashed lines) with a larger frequency shift for more acoustic dispersion relations (blue to red data).
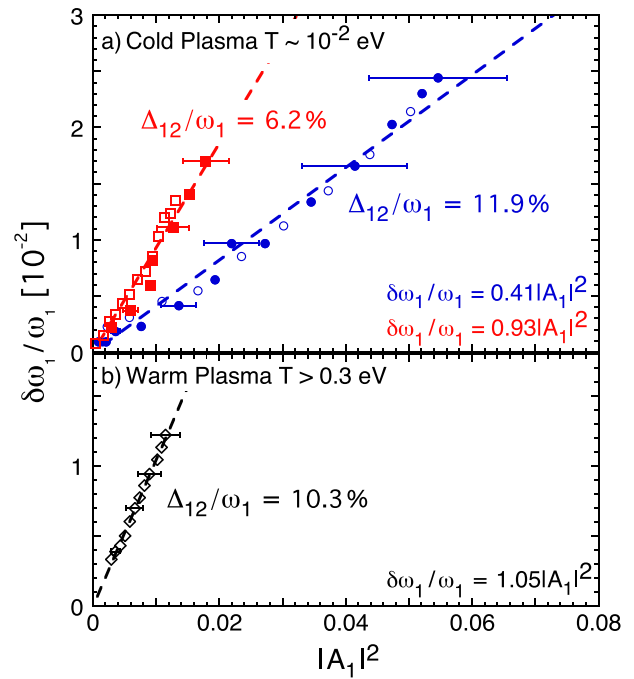
Combining Eqs. (13) and (15), theory predicts

$$\delta\omega_1/\omega_1 \approx (3/8)R|A_1^{(2)}| \qquad (16)$$

that the nonlinear frequency shift is proportional to the amplitude of the second harmonic $|A_1^{(2)}|$. In Sec. IV, we showed that $|A_1^{(2)}|$ is underestimated by cold fluid theory, so a corresponding underestimate of $\delta\omega_1/\omega_1$ would be expected. However, Eqs. (15) and (16) predict nonlinear frequencies about a factor of 2 larger than the measurements.

This discrepancy suggests the presence of other nonlinear effects that reduce the measured wave frequency. Previous fluid theory[7] found that the ponderomotive force of the wave redistributes particles axially, creating a nonlinear radial eigenfunction and causing a negative nonlinear frequency shift. Equation (15) assumes a constant radial eigenfunction and therefore neglects this negative frequency shift. Reference 7 predicts $\delta\omega_1/\omega_1 \sim -0.05(A_1)^2$ for a plasma extending radially out to the wall with no harmonic content. The addition of this negative shift alone does not explain the observed discrepancy in $\delta\omega_1/\omega_1$, but this ponderomotive effect may be enhanced by the steepening of the waveform. Finite length effects may also contribute to the smaller observed frequency shift. These theories[4,7] are periodic in z and therefore neglect a possible downward frequency shift resulting from the elongation of the plasma due to these large amplitude waves.

These measured nonlinear frequency shifts are also temperature dependent. Figure 5(b) shows a factor 2.5 increase in $\delta\omega_1/\omega_1$ as the plasma temperature is increased from $10^{-2}$ to 0.55 eV with a corresponding reduction in $\Delta_{12}/\omega_1$ from 11.9% to 10.3%. As discussed in Sec. IV, warm plasmas have a stronger harmonic content, so this larger frequency shift is in qualitative agreement with cold fluid theory predicting $\delta\omega_1/\omega_1 \propto A_1^{(2)}$. We note that for these warm plasmas,

Eq. (15) is within 10% of the measured frequency shift, but we believe that this correspondence is merely a coincidence since cold fluid theory underestimates the harmonic content of these warm plasmas.

The competition between positive and negative nonlinear frequency shifts is most evident in large amplitude $m_z = 2$ waves. At low temperatures $T \lesssim 10^{-2}$ eV, the negative frequency shift dominates, and $\omega_2$ decreases with $|A_2|$ as shown in Fig. 6. However, at higher temperatures $T \gtrsim 10^{-2}$ eV, $\delta\omega_2/\omega_2$ changes sign, possibly due to the stronger harmonic content.

Previous experiments[8] on pure electron plasmas observed a similar competition between positive and negative frequency shifts. For lower order modes $m_z \leq 3$, a positive frequency shift was observed. However, for higher order modes $m_z > 3$, which have a weaker harmonic content, $\delta\omega/\omega$ was negative. Further experiments and theory are required to fully understand these nonlinear frequency shifts.

## VI. THE DECAY INSTABILITY, SLOW AVERAGE GROWTH, AND OSCILLATORY COUPLING

In this section, the stability of these nonlinear waves with respect to small perturbations of the waveform is investigated on cold plasmas $T \lesssim 10^{-2}$ eV. We focus on the common parametric instability in which a large amplitude pump wave decays to two longer wavelength daughter waves each at nearly half the pump wave frequency. For this TG dispersion relation, this near resonance condition is satisfied by a large $m_z = 2$ wave with a small $m_z = 1$ perturbation.

For large amplitudes ($|A_2| \gtrsim 30\%$, $\Gamma_0/\Delta_{12} \gtrsim 0.7$), Fig. 7(a) shows that the $m_z = 2$ pump wave (dashed curve) is unstable to the parametric instability. Again, $\Gamma_0$ is the scaled pump wave amplitude, which describes the strength of the nonlinear coupling between the pump and daughter wave. The $m_z = 1$ daughter wave (solid curve) grows exponentially out of the noise at a rate $\Gamma_E = 7443$ s$^{-1}$ and phase-locked with a relative phase $\theta_{12} = -0.73\pi$. However, the pump and daughter waves do not completely exchange energy. When $|A_1^{max}| \sim 0.6|A_2^{max}|$, the direction of energy exchange reverses, and the
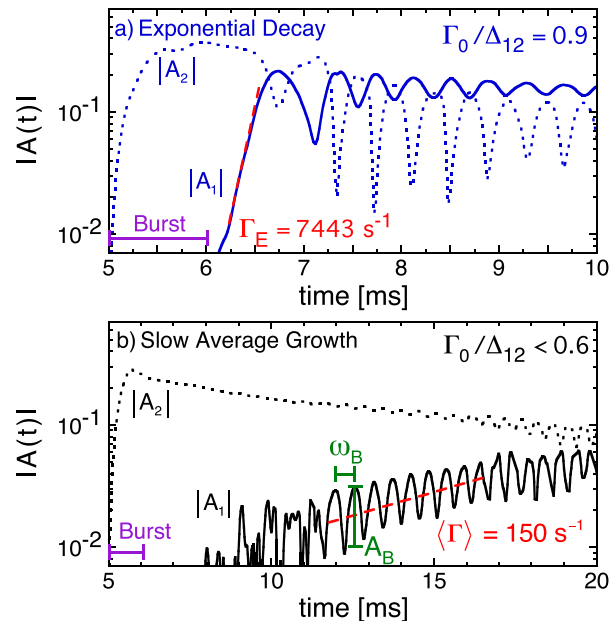


**FIG. 7.** (a) Above a threshold pump wave amplitude, the parametric instability is observed. However, below threshold (b), the pump wave modulates the daughter wave amplitude with a slow average growth not predicted by fluid analyses.

pump and daughter wave amplitudes proceed to oscillate as the waves exchange energy back and forth. At late times, the daughter wave amplitude is dominant with $\langle A_1 \rangle / \langle A_2 \rangle \sim 2$. Energy is removed from both waves through collisional drag damping[47] at a rate $\gamma \sim 50$ s$^{-1}$ for $T \sim 10^{-2}$ eV.

In contrast, moderate amplitude ($20\% \lesssim |A_2| \lesssim 30\%$, $\Gamma_0/\Delta_{12} \sim 0.6$) pump waves have only a weak instability [Fig. 7(b)]. The average $m_z = 1$ amplitude grows slowly $\langle \Gamma \rangle \lesssim 500$ s$^{-1}$ with amplitude modulations $A_B \propto |A_2|$ at a rate $\omega_B \sim \Delta_{12}$. These modulations are a result of the daughter wave being driven in-and-out of phase by the pump wave, which we refer to as oscillatory coupling. Although this oscillatory coupling is predicted by both three-wave and N-wave fluid analyses, the slow average growth is not. A similar weak instability is observed in kinetic particle-in-cell (PIC) simulations as particles slowly become trapped in the wave potential (see Sec. IX).

For small wave amplitudes ($|A_2| \lesssim 20\%$, $\Gamma_0/\Delta_{12} \lesssim 0.5$), the daughter wave is stable. Oscillatory coupling is still observed, but the slow average growth mechanism is either suppressed or is at a rate weaker than the damping rate, so the average $m_z = 1$ amplitude decreases slowly with time. This behavior has been observed in previous experiments[48] by initially driving the daughter wave above the noise floor with an additional $m_z = 1$ seed burst added to the drive.

## VII. THREE-WAVE THEORY

Although harmonics of the pump and daughter waves are ignored in a three-wave analysis, several properties of the instability can be understood through this simpler theory. Three-wave, cold fluid theory[35] characterizes this instability by the scaled pump wave amplitude $\Gamma_0$ and frequency detuning $\Delta_{12}$. This theory keeps the nonlinear
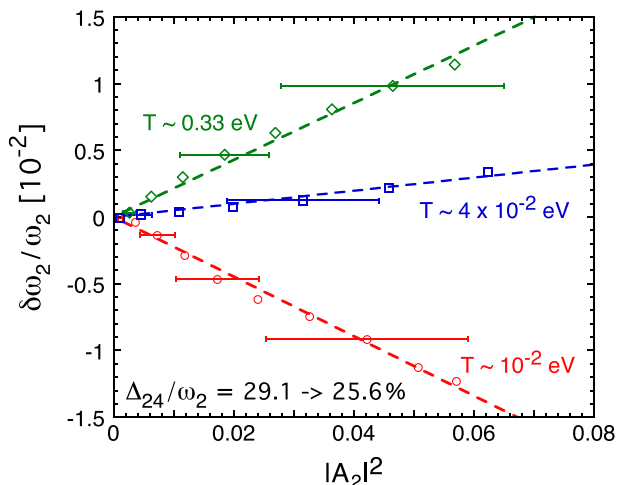


**FIG. 6.** Percent change in the frequency of a large amplitude $m_z = 2$ wave for various temperatures. The observed negative frequency shift is not predicted by current fluid theory. Dashed lines are fits to the wave amplitude squared.

terms in the fluid equations and uses a two time scale analysis for the density perturbation

$$\Psi(t) = \Psi_1^{(1)}(t) + \Psi_2^{(1)}(t) \qquad (17)$$

to derive the coupled amplitude equations

$$\dot{A}_1 = -iXA_2 A_1^* e^{i\Delta_{12}t},$$
$$\dot{A}_2 = -iX(A_1)^2 e^{-i\Delta_{12}t}, \qquad (18)$$

where $X = \Gamma_0/|A_2| = (3R/8)\omega_1$ is the nonlinear coupling coefficient.

### A. Small daughter wave approximation

In the limit $|A_1| \ll |A_2|$, $|\dot{A}_2| \approx 0$, and these coupled equations can be solved analytically to find

$$A_1(t) = \alpha e^{(\Gamma + i\Delta_{12}/2)t} + \beta e^{-(\Gamma - i\Delta_{12}/2)t}, \qquad (19)$$

where $\Gamma = \sqrt{\Gamma_0^2 - (\Delta_{12}/2)^2}$, and $\alpha$ and $\beta$ are constants. Plugging this solution back into Eq. (18), we find

$$\beta = -\alpha^* \frac{\Gamma_0}{|\Gamma| + \Delta_{12}/2}. \qquad (20)$$

The constant $\alpha$ is set by the initial conditions.

Equation (19) predicts two different behaviors for the time evolution of the $m_z = 1$ amplitude. For $\Gamma_0 > \Delta_{12}/2$, $\Gamma$ is real, and the daughter wave amplitude is composed of an exponentially growing and decaying solution. This predicts the exponential growth rate $\Gamma_E = \Gamma$ of Fig. 7(a). In contrast, for $\Gamma_0 < \Delta_{12}/2$, $\Gamma$ is imaginary, and the daughter wave amplitude is predicted to oscillate with excursions $A_B = \Gamma_0 \langle A_1 \rangle /(|\Gamma| + \Delta_{12}/2)$ at a frequency $\omega_B = 2|\Gamma|$ similar to the behavior of Fig. 7(b) but around a constant average amplitude $\langle A_1 \rangle$. This modulation of the daughter wave amplitude results from the same mode coupling that causes the exponential growth and occurs at the oscillatory coupling rate (OCR)

$$\Gamma_{OCR} \equiv \frac{A_B}{\langle A_1 \rangle} \omega_B = \Gamma_0 \frac{2|\Gamma|}{|\Gamma| + \Delta_{12}/2}. \qquad (21)$$

In Fig. 8(a), the measured (symbols) and three-wave theory predicted (curves) $\Gamma_{OCR}$ and $\Gamma_E$ are plotted vs the pump wave amplitude $|A_2|$ for two cold plasmas with different $\Delta_{12}/\omega_1$ values. The experimentally determined oscillatory coupling rates (open symbols) are calculated from Eq. (21) through measurements of the amplitude $A_B$, frequency $\omega_B$, and average $\langle A_1 \rangle$ of the modulated daughter wave amplitude in short time segments during a single slow growth evolution of the daughter wave [Fig. 7(b)]. For a given pump wave amplitude $|A_2|$, $\Gamma_{OCR}$ is weaker for the plasma with $\Delta_{12}/\omega_1 = 6.2\%$, in agreement with three-wave theory.[35] This smaller $\Gamma_{OCR}$ results from the reduction of $\omega_1$ and hence $\Gamma_0$ as the plasma aspect ratio is increased (see Fig. 2).

Above a threshold pump wave amplitude (arrows), a transition to exponential growth (closed symbols) is observed. These exponential growth rates are measured by fitting an exponentially growing sine wave to the digitized wall signal [Fig. 7(a)] as the daughter wave grows out of the noise. In general, the rates $\Gamma_E \sim 3000 - 9000$ s$^{-1}$ are
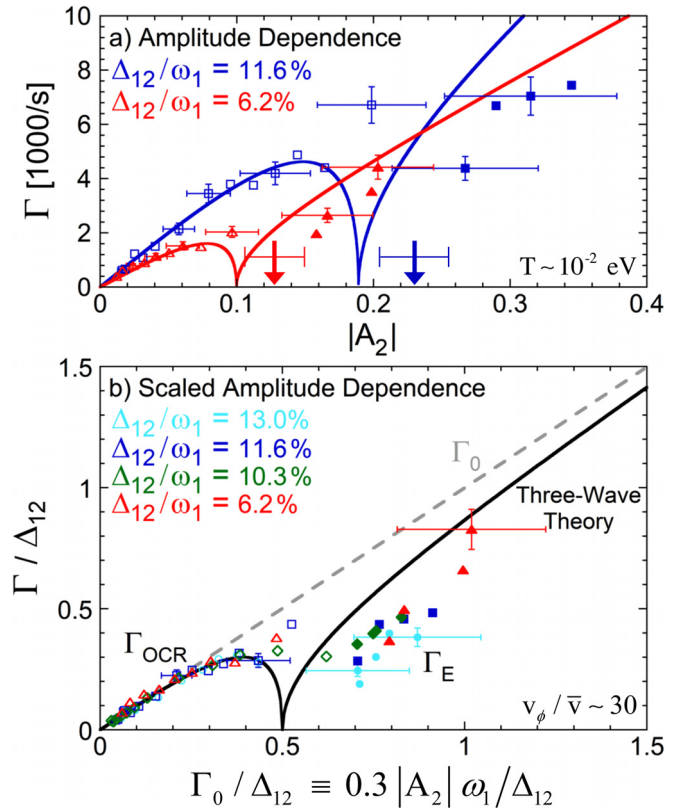


**FIG. 8.** (a) Measurements of the oscillatory coupling (open symbols) and exponential growth (closed symbols) rates vs the pump wave amplitude $|A_2|$ for two cold plasmas with different $\Delta_{12}/\omega_1$ values. (b) Rates normalized to $\Delta_{12}$ vs the scaled pump wave amplitude for four different $\Delta_{12}/\omega_1$ values. Solid curves are three-wave theory.

obtained from fits over $5 - 10$ cycles of the growing $m_z = 1$ wave, and during this growth, the $m_z = 2$ amplitude is about 20 times the $m_z = 1$ amplitude. The measured exponential growth rates are about 30% lower in magnitude than the three-wave theory prediction. As the plasma becomes more acoustic (blue to red), the $m_z = 2$ amplitude required for exponential growth is reduced in rough agreement with three-wave theory.[35]

This three-wave theory[35] predicts that the $\Gamma_{OCR}$ and $\Gamma_E$ dependence on $\Delta_{12}/\omega_1$ is removed by expressing the pump wave amplitude in terms of the dimensionless parameter $\Gamma_0/\Delta_{12} \propto |A_2|\omega_1/\Delta_{12}$ and scaling the rates $\Gamma$ by the detuning $\Delta_{12}$. The measured (symbols) and predicted (black curve) rates shown in Fig. 8(b) reflect this scaling for four cold plasmas with different degrees of acoustic dispersion. For $\Gamma_0/\Delta_{12} < 0.4$, $\Gamma_{OCR}$ is in quantitative agreement with three-wave theory[35] (black curve) independent of $\Delta_{12}/\omega_1$. The predicted reduction in $\Gamma_{OCR}$ near $\Gamma_0/\Delta\omega \sim 0.5$ reflects $\omega_B \rightarrow 0$ as the infinitesimal daughter wave becomes phase-locked with the pump. It is unclear whether the larger measured $\Gamma_{OCR}$ near the decay threshold is a result of the finite amplitude of the daughter waves or of the observed harmonic content, which is ignored in this three-wave analysis.[35] For $\Gamma_0/\Delta_{12} \gtrsim 0.7$, the measured $\Gamma_E$ in Fig. 8 is about 30% lower in

magnitude than the three-wave theory (black curve) for the various $\Delta_{12}/\omega_1$ values.

## B. Phase space analysis

In this section, a phase space analysis[35,36] is used to study the time evolution of the coupled amplitude equations. Using $A_m(t) = |A_m(t)|e^{i\phi_m(t)}$, Eq. (18) can be written in terms of the wave amplitude and phase difference as

$$|\dot{A}_1| = -X|A_1||A_2|\sin(\theta_{12}), \tag{22a}$$

$$|\dot{A}_2| = X|A_1|^2\sin(\theta_{12}), \tag{22b}$$

$$\dot{\theta}_{12} = -\left[2X|A_2| - X\frac{|A_1|^2}{|A_2|}\right]\cos(\theta_{12}) - \Delta_{12}, \tag{22c}$$

where $\theta_{12} = 2\phi_1 - \phi_2 - \Delta_{12}t$ is the phase difference between the pump and daughter wave. Combining Eqs. (22a) and (22b) to eliminate the $\sin(\theta_{12})$ term, the Manley-Rowe relation

$$|A_1|^2 + |A_2|^2 \equiv A^2 \tag{23}$$

is obtained, where $A$ is a constant. Equation (23) is equivalent to the conservation of wave energy. Of course, damping is neglected in this theory, and experimentally, the waves lose energy through collisional drag.[47]

Normalizing the time by the maximum coupling strength $\bar{t} = XAt$, and substituting in Eq. (23) to eliminate $|A_1|$, Eq. (22c) simplifies to

$$\dot{\theta}_{12} = \left[\frac{1}{x} - 3x\right]\cos(\theta_{12}) - \eta, \tag{24}$$

where $x \equiv |A_2|/A$ is the fraction of energy in the pump wave and $\eta \equiv \Delta_{12}/XA$ is the detuning normalized to the maximum coupling strength. In the limit $|A_1| \ll |A_2|$, $A \approx |A_2|$, and $\eta \approx \Delta_{12}/\Gamma_0$. The daughter wave amplitude $|A_1|$ is also eliminated from Eq. (22b) through the substitution of Eq. (23) to obtain

$$\dot{x} = [1 - x^2]\sin(\theta_{12}). \tag{25}$$

Equations (24) and (25) describe the time evolution of the phase space $(\theta_{12}, x)$, where $\eta$ determines the topology.

Figure 9 (top) shows a schematic of the phase space in the oscillatory coupling regime ($\eta > 2$). The phase space is characterized by two jump points located at $J_1 = (-\pi/2, 0)$ and $J_2 = (\pi/2, 0)$ and a center fixed point at $(0, x_0)$, where

$$x_0 = -\frac{\eta}{6} + \sqrt{\left(\frac{\eta}{6}\right)^2 + \frac{1}{3}}. \tag{26}$$

The red curve connecting $J_1$ and $J_2$ is a separatrix contour. For $x \sim 1$, the pump wave is stable and only undergoes small oscillations (blue contours) as the phase difference oscillates through $2\pi$. The size of these oscillations is increased when the pump and daughter wave are of comparable amplitude $\left(x \sim 1/\sqrt{2}\right)$. Again, this theory assumes that the wave energy is conserved [Eq. (23)], so a decrease in $x$ (i.e., $|A_2|$) reflects an increase in $|A_1|$ and vice versa. Within the separatrix (red contour), $|A_1| > |A_2|$, and the pump wave undergoes the dominant amplitude modulations.
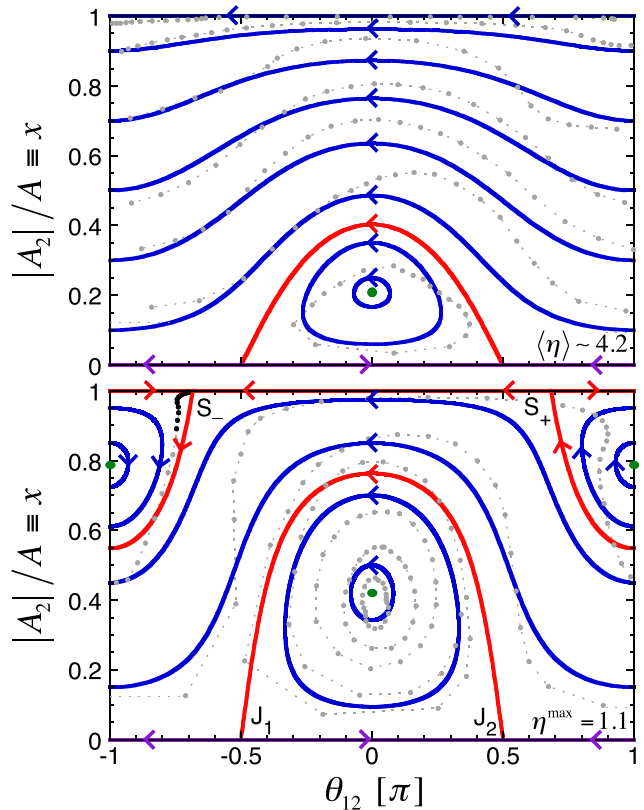


**FIG. 9.** A schematic of the phase space describing the coupled amplitude equations of the parametric instability in both the oscillatory coupling (top) and exponential growth (bottom) regimes. Solid curves are theory, and gray symbols are experimental measurements.

The gray symbols of Fig. 9 (Top) correspond to phase space measurements in the oscillatory coupling regime for the data shown in Fig. 7(b). For each amplitude oscillation, the phase space measurements are in rough agreement with three-wave theory. However, the unexpected, weak instability [Fig. 7(b)] slowly transfers energy to the daughter wave, and the measured phase space contours spiral toward the center fixed point located at $(0, x_0)$. For clarity, we have only plotted the measured contours for a few values of $x$. The three-wave predicted topology shown if Fig. 9 (top) is for the average measured $\eta$, since experimentally $\eta$ is not a constant due to damping of the waves.

In the exponential growth regime ($\eta < 2$), the phase space topology changes, as shown in Fig. 9 (bottom). Two new center fixed points are located at $(\pm\pi, x_\pi)$, where

$$x_\pi = \frac{\eta}{6} + \sqrt{\left(\frac{\eta}{6}\right)^2 + \frac{1}{3}}. \tag{27}$$

Around these center fixed points are two new separatrix contours described by

$$x = -\frac{\eta}{2}\cos(\theta_{12}) \tag{28}$$

for $2 > -2\cos(\theta_{12}) > \eta$ with saddle points located at $S_\pm = (\pm\theta_s, 1)$, where $\cos(\theta_s) = -\eta/2$. In this phase space, a pump wave with a small

$m_z = 1$ perturbation ($x \sim 1$) decays with a nearly constant phase difference as $S_-$ is approached along the separatrix contour. This is the exponential decay instability discussed in Sec. VII A. During this process, the pump wave continues to exchange energy with the daughter wave until $(-\pi, \eta/2)$ at which point the direction of energy exchange reverses along the $S_+$ separatrix contour, and the process repeats. Within the lower separatrix of this phase space, the solutions are characterized by large modulations of the pump wave amplitude with an average amplitude centered around $x_0$.

The experimental measurements of the phase space in the exponential growth regime [Fig. 7(a)] are shown as the black and gray symbols of Fig. 9 (Bottom). The black symbols correspond to the initial exponential growth of the daughter wave. Here, the theory contours correspond to the measured $\eta^{\text{max}}$ to better capture the initial exponential growth behavior. Like in the oscillatory coupling regime, the measured phase space contours (gray symbols) spiral toward the center fixed point at $(0, x_0)$. This behavior is not predicted by three-wave theory but explains the observation that at late times, $\langle A_1 \rangle \sim 2\langle A_2 \rangle$ since this ratio of amplitudes is roughly $x_0$.

Figure 10 shows a more detailed analysis of the decay instability. For $|A_1| \ll |A_2|$, exponential growth occurs at the $S_-$ saddle point, so the daughter wave is predicted to be phase-locked to the pump wave with a phase difference

$$\theta_{12} \equiv \theta_s = -\arccos\left(\frac{-\Delta_{12}}{2\Gamma_0}\right) \qquad (29)$$

[black curve of Fig. 10(a)]. The magnitude of the measured $\theta_{12}$ is initially larger than the three-wave theory prediction for various $\Delta_{12}/\omega_1$, but approaches three-wave theory at large pump amplitudes.

This phase space analysis[35,36] also shows that the frequency detuning $\Delta_{12}$ moderates the amount of energy exchanged between the unstable pump and growing daughter wave. When the pump wave decays, it only exchanges part of its energy with the daughter wave. Three-wave theory predicts that the daughter wave reaches a maximum amplitude of

$$\frac{|A_1^{\text{max}}|}{A} = \sqrt{1 - \left(\frac{\Delta_{12}}{2\Gamma_0}\right)^2} \qquad (30)$$

[black curve of Fig. 10(b)] before the direction of energy exchange reverses. That is to say, the instability threshold is predicted to be a gradual transition with a majority of energy transfer $|A_1^{\text{max}}| \gtrsim 0.9|A_2^{\text{max}}|$ only for $\Gamma_0/\Delta_{12} \gtrsim 1.1$. Experimentally, we find near complete energy exchange ($|A_1^{\text{max}}|/|A_2^{\text{max}}| \sim 1$) at pump wave amplitudes smaller than the three-wave prediction even though the measured decay threshold is slightly suppressed.

## VIII. N-WAVE THEORY

This rough but broad correspondence between the experiments and simple three-wave theory of the instability is surprising. We showed in Sec. IV that these waves are not single sinusoidal oscillations as three-wave theory assumes but instead contain harmonics of the fundamental waves. When these harmonics are included in the instability analysis, fluid theory[4] predicts that the three-wave parametric instability is eliminated in traveling pump waves, analogous to the stability of solitary-wave solutions of the Korteweg-de-Vries[37] and Boussinesq[38] equations. In contrast, for the standing waves of interest in these experiments, the parametric instability is predicted[4] to be suppressed but not eliminated by the addition of wave harmonics.

For a plasma with $\Delta_{12}/\omega_1 = 7.6\%$ ($k_\perp = 6$ in the notation of Ref. 4), this N-wave, cold fluid theory predicts an exponential instability for $\Gamma_0/\Delta_{12} \gtrsim 1.5$ with growth rates a factor of 5 weaker than the three-wave theory prediction. These results are in stark contrast to the experimentally measured growth rates, which are only about 30% weaker than three-wave theory and occur for $\Gamma_0/\Delta_{12} \gtrsim 0.7$ [Fig. 8(b)]. Also, this N-wave analysis predicts further suppression of the instability as the dispersion relation becomes more acoustic. However, experimentally we observe little dependence on $\Delta_{12}/\omega_1$ beyond the predicted three-wave theory behavior. Fluid simulations have been conducted to include the effects of finite length, pressure, and radial dependence to closely match the experimental conditions. However, these fluid effects alone seem to be unable to match the observed instability.

## IX. DESTABILIZATION FROM TRAPPED PARTICLES

However, recent kinetic theory[42] and simulations are able to produce growth rates similar to the experiments when a small fraction of trapped particles are included. These trapped particles destabilize the wave because they exhibit negative compressibility. In the instability, adjacent peaks of the wave train approach one-another and therefore recede from the next peaks. Normally, the density and pressure of
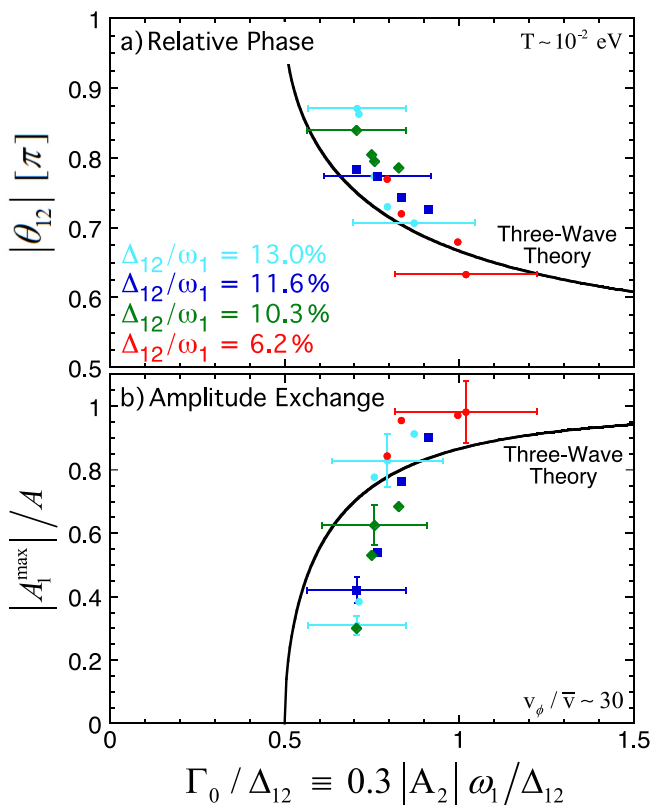


**FIG. 10.** Measurements (symbols) and theory (black curves) of the relative phase difference (a) between the pump and daughter wave at the start of exponential growth, and the maximum daughter wave amplitude (b) reached at the end of this energy exchange.

particles trapped between approaching peaks would increase and would decrease for particles trapped between receding peaks, producing a restoring force that stabilizes these modulations. Trapped particles with energies just below the approaching wave peaks, however, gain sufficient energy to become passing and are then retrapped between receding peaks. The net effect of these marginally trapped particles is to reverse the sign of the trapped particle density and pressure change, which produces a force that amplifies the modulation when the trapped particle fraction is sufficiently large $f_T \gtrsim 0.1\%$. For a more detailed explanation of this process, we refer the reader to Ref. 49 in which the theory of the parametric instability mechanism caused by particles that are weakly trapped is discussed.

For these cold plasmas ($v_\phi/\bar{v} \gtrsim 5$), this trapped particle fraction has not yet been experimentally observed; however, the presence of a small fraction of trapped particles is not unreasonable. Near the decay threshold ($|A_2| \sim 25\%$), the trapping region is large with a half-width $v_T = v_\phi\sqrt{2|A_2|} \sim 20\bar{v}$ for $v_\phi/\bar{v} \sim 30$. Also, finite length (r, z) PIC simulations[49] predict that the driver used to excite these waves creates a small population of highly energetic, trapped particles. In these PIC simulations, these trapped particles cause the anomalous slow average growth [Fig. 7(b)] as the trapped particle population gradually increases. However, to obtain the strong exponential growth [Fig. 7(a)] observed experimentally, these PIC simulations require a larger fraction of trapped particles than produced by the driver alone.

To investigate this trapped particle mechanism, experiments are conducted at higher temperatures ($3.5 \lesssim v_\phi/\bar{v} \lesssim 5$), where trapped particles are ubiquitous. At these high temperatures, small amplitude waves ($|A_m| \lesssim 0.1\%$) damp at the linear Landau rate[50] $8000 \gtrsim \gamma_L \gtrsim 50$ s$^{-1}$. However, at large wave amplitudes, resonant particles are trapped in the wave potential resulting in trapping oscillations at a frequency $\omega_T^2 \sim |A_m|\omega^2$ and diminishing the damping rate as the trapped particles phase mix producing a BGK state.[46,51] The large amplitude kinetic pump waves of these experiments have weak damping $\gamma \sim 100$ s$^{-1}$, presumably resulting from the collisional repopulation of the plateau in the velocity distribution.

Experimentally, we find that these kinetic pump waves are more unstable with respect to decay to longer wavelength, consistent with recent kinetic theory[42] of the trapped particle mechanism. Figure 11(a) shows the measurements of the decay instability at four different temperatures. At low temperatures ($v_\phi/\bar{v} \gtrsim 5$), the instability threshold is roughly determined by $\Gamma_0/\Delta\omega \sim 0.6$. In contrast, for a plasma with $v_\phi/\bar{v} \sim 3.5$, we observe similar exponential growth rates as for a cold plasma but at half the pump wave amplitude, i.e., $\Gamma_0/\Delta\omega \sim 0.3$. This reduction in the instability threshold is inconsistent with fluid theories but is in qualitative agreement with kinetic theory that includes the effect of trapped particles. Previous qualitative experimental work[21] investigating the decay instability of higher axial modes on hot electron plasmas observed a similar temperature dependent reduction of the instability threshold, and we note that preliminary experiments[52] presented by us missed this temperature dependence as these early experiments were conducted in a regime (large detuning and a strong $m_z = 1$ seed) where the instability threshold was obfuscated by slow average growth.

Shown in Fig. 11(b) are periodic (r, z, $v_z$) drift-kinetic Poisson (squares) and (r, z) PIC (triangles) simulations of the decay. At low temperatures ($v_\phi/\bar{v} \sim 8.9$), these kinetic simulations observe both OCR and exponential growth rates near cold fluid, three-wave theory,
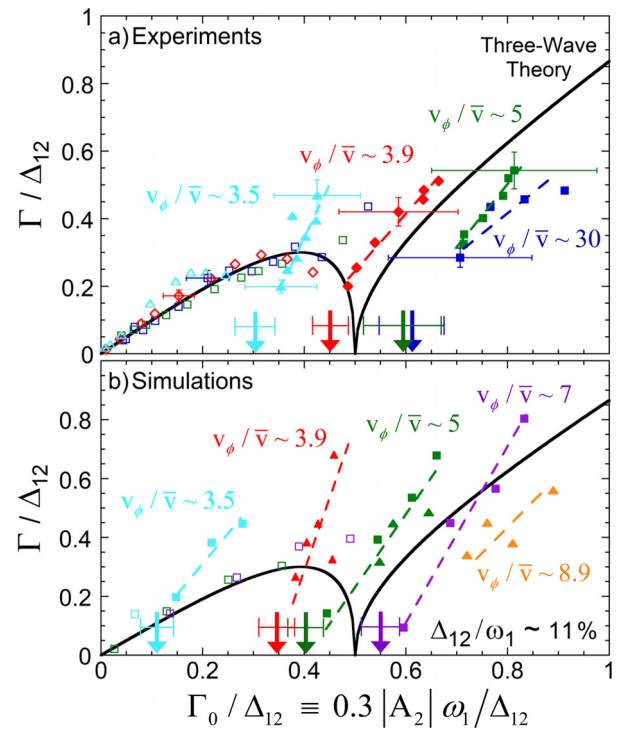


**FIG. 11.** Measurements (a) and simulations (b) of OCR and exponential growth rates at different plasma temperatures. The reduction in the instability threshold (arrows) at higher temperatures (lower $v_\phi/\bar{v}$) contradicts fluid theories.

consistent with the experiments. However, it is the trapped particles in these simulations that cause the instability. The pump wave is stable if the trapped particle population is artificially eliminated by setting $F(r, z, v_z, t) = 0$ for $|v_z| > 4.5\bar{v}$ at every r, z, and time step t. However, when the fraction of trapped particles is increased in these simulations by increasing the plasma temperature, the pump wave goes unstable at even lower amplitudes than experimentally observed.

## X. CONCLUSION

At large wave amplitudes, harmonics of the fundamental TG wave are generated. For cold plasmas, the amplitude of the $j$th harmonic is proportional to the fundamental amplitude to the $j$th power, and the proportionality factor increases as the dispersion relation becomes more acoustic, in qualitative agreement with cold fluid theory.[4] These harmonics are predicted to cause a positive nonlinear frequency shift of the fundamental.[4] However, experimentally, the frequency shift is smaller than the current theory prediction, even negative for some cases, suggesting another nonlinear mechanism. At higher temperatures, both the harmonic content and nonlinear frequency shift are observed to increase. Further experiments and theory will be needed to understand this temperature dependence.

When these harmonics are included in a fluid analysis of the stability of these nonlinear waves, the parametric instability is suppressed compared to a standard three-wave theory. However, the experiments show a rough but broad correspondence to this simpler three-wave analysis. Oscillatory coupling rates are in quantitative agreement with

three-wave theory, and the exponential growth rates are only slightly reduced.

This discrepancy between the N-wave analysis and experiments is resolved by the inclusion of weakly trapped particles. Recent kinetic theory and simulations show that a small fraction of wave-trapped particles destabilizes the pump wave, enabling the exponential growth of longer wavelength waves. Experiments and simulations show stronger growth with increasing plasma temperature and decreasing $v_\phi/\bar{v}$. Incisively, the simulations show the cessation of instability when particles near $v_\phi$ are removed.

These experiments have focused on nonlinear processes for a particular system, i.e., TG waves. However, the observed fluid nonlinearities should be generally applicable to waves with a similar linear dispersion relation, such as cold magnetized plasma waves in a uniform plasma, IAWs, and shallow water waves in the Boussinesq approximation. The instability resulting from weakly trapped particles may also be active in IAWs, where kinetic simulations[28,43] show instability threshold reduced from standard fluid theory predictions.

## ACKNOWLEDGMENTS

## REFERENCES

[1]J. A. C. Cabral, L. M. Lapão, and J. T. Mendonça, Phys. Fluids B: Plasma Phys. **5**, 787 (1993).

[2]W. Bertsche, J. Fajans, and L. Friedland, AIP Conf. Proc. **692**, 22 (2003).

[3]F. Peinetti, W. Bertsche, J. Fajans, J. Wurtele, and L. Friedland, Phys. Plasmas **12**, 062112 (2005).

[4]D. H. E. Dubin and A. Ashourvan, Phys. Plasmas **22**, 102102 (2015).

[5]R. L. Berger, S. Brunner, T. Chapman, L. Divol, C. H. Still, and E. J. Valeo, Phys. Plasmas **20**, 032107 (2013).

[6]T. Chapman, R. L. Berger, S. Brunner, and E. A. Williams, Phys. Rev. Lett. **110**, 195004 (2013).

[7]B. M. Lamb and G. J. Morales, Phys. Fluids **26**, 3488 (1983).

[8]Y. Yamazawa and T. Michishita, Jpn. J. Appl. Phys. **40**, 5431 (2001).

[9]R. Z. Sagdeev and A. A. Galeev, *Nonlinear Plasma Theory* (W. A. Benjamin, New York, 1969).

[10]R. N. Franklin, Rep. Prog. Phys. **40**, 1369 (1977).

[11]F. W. Perkins and J. Flick, Phys. Fluids **14**, 2012 (1971).

[12]M. N. Rosenbluth, Phys. Rev. Lett. **29**, 565 (1972).

[13]M. Porkolab, Fusion Eng. Des. **12**, 93 (1990).

[14]J. F. Drake, P. K. Kaw, Y. C. Lee, G. Schmid, C. S. Liu, and M. N. Rosenbluth, Phys. Fluids **17**, 778 (1974).

[15]M. Porkolab, S. Bernabei, W. M. Hooke, R. W. Motley, and T. Nagashima, Phys. Rev. Lett. **38**, 230 (1977).

[16]Y. Takase, M. Porkolab, J. J. Schuss, R. L. Watterson, C. L. Fiore, R. E. Slusher, and C. M. Surko, Phys. Fluids **28**, 983 (1985).

[17]S. Baek, R. Parker, S. Shiraiwa, G. Wallace, P. Bonoli, D. Brunner, I. Faust, A. Hubbard, B. LaBombard, and M. Porkolab, Plasma Phys. Controlled Fusion **55**, 052001 (2013).

[18]F. S. McDermott, G. Bekefi, K. E. Hackett, J. S. Levine, and M. Porkolab, Phys. Fluids **25**, 1488 (1982).

[19]A. A. Kabantsev, Y. A. Tsidulko, and C. F. Driscoll, Phys. Rev. Lett. **112**, 055003 (2014).

[20]A. A. Kabantsev, F. Valentini, and C. F. Driscoll, AIP Conf. Proc. **862**, 13 (2006).

[21]H. Higaki, Plasma Phys. Controlled Fusion **39**, 1793 (1997).

[22]H. Bandulet, C. Labaune, K. Lewis, and S. Depierreux, Phys. Rev. Lett. **93**, 035002 (2004).

[23]C. Niemann, S. H. Glenzer, J. Knight, L. Divol, E. A. Williams, G. Gregori, B. I. Cohen, C. Constantin, D. H. Froula, D. S. Montgomery, and R. P. Johnson, Phys. Rev. Lett. **93**, 045004 (2004).

[24]R. Stenzel and A. Y. Wong, Phys. Rev. Lett. **28**, 274 (1972).

[25]S. Dorfman and T. A. Carter, Phys. Rev. Lett. **116**, 195002 (2016).

[26]S. J. Karttunen, J. N. McMullin, and A. A. Offenberger, Phys. Fluids **24**, 447 (1981).

[27]B. I. Cohen, B. F. Lasinski, A. B. Langdon, and E. A. Williams, Phys. Plasmas **4**, 956 (1997).

[28]T. Chapman, S. Brunner, J. Banks, R. Berger, B. Cohen, and E. Williams, Phys. Plasmas **21**, 042107 (2014).

[29]D. Pesme, C. Riconda, and V. Tikhonchuk, Phys. Plasmas **12**, 092101 (2005).

[30]B. Cohen, E. Williams, R. Berger, D. Pesme, and C. Riconda, Phys. Plasmas **16**, 032701 (2009).

[31]A. Ng, L. Pitt, D. Salzmann, and A. A. Offenberger, Phys. Rev. Lett. **42**, 307 (1979).

[32]C. E. Clayton, C. Joshi, and F. F. Chen, Phys. Rev. Lett. **51**, 1656 (1983).

[33]J. E. Bernard and J. Meyer, Phys. Rev. Lett. **55**, 79 (1985).

[34]S. H. Glenzer, L. M. Divol, R. L. Berger, C. Geddes, R. K. Kirkwood, J. D. Moody, E. A. Williams, and P. E. Young, Phys. Rev. Lett. **86**, 2565 (2001).

[35]A. Ashourvan, Ph.D. dissertation, UCSD, 2014.

[36]J. A. Armstrong, N. Bloembergen, J. Ducuing, and P. S. Pershan, Phys. Rev. **127**, 1918 (1962).

[37]T. B. Benjamin, Proc. R. Soc. London, Ser. A **328**, 153 (1972).

[38]J. L. Bona and R. L. Sachs, Commun. Math. Phys. **118**, 15 (1988).

[39]D. H. E. Dubin, Phys. Plasmas **26**, 102111 (2019).

[40]M. S. Longuet-Higgins, Proc. R. Soc. London, Ser. A **360**, 471 (1978).

[41]M. S. Longuet-Higgins, Proc. R. Soc. London, Ser. A **360**, 489 (1978).

[42]D. H. E. Dubin, Phys. Rev. Lett. **121**, 015001 (2018).

[43]T. Chapman, R. L. Berger, B. I. Cohen, J. W. Banks, and S. Brunner, Phys. Rev. Lett. **119**, 055002 (2017).

[44]F. Anderegg, X.-P. Huang, E. Sarid, and C. Driscoll, Rev. Sci. Instrum. **68**, 2367 (1997).

[45]A. Trivelpiece and R. Gould, J. Appl. Phys. **30**, 1784 (1959).

[46]J. Danielson, F. Anderegg, and C. Driscoll, Phys. Rev. Lett. **92**, 245003 (2004).

[47]M. Affolter, F. Anderegg, D. H. E. Dubin, and C. F. Driscoll, Phys. Plasmas **25**, 055701 (2018).

[48]M. Affolter, F. Anderegg, D. H. E. Dubin, F. Valentini, and C. F. Driscoll, Phys. Rev. Lett. **121**, 235004 (2018).

[49]D. H. E. Dubin, Phys. Plasmas **26**, 102113 (2019).

[50]M. Affolter, F. Anderegg, D. H. E. Dubin, and C. F. Driscoll, Phys. Rev. Lett. **117**, 155001 (2016).

[51]I. B. Bernstein, J. M. Greene, and M. D. Kruskal, Phys. Rev. **108**, 546 (1957).

[52]F. Anderegg, M. Affolter, A. Ashourvan, D. H. E. Dubin, F. Valentini, and C. F. Driscoll, AIP Conf. Proc. **1668**, 020001 (2015).